Journal of Materials Chemistry A

ROYAL SOCIETY OF CHEMISTRY

PAPER

View Article Online
View Journal | View Issue

Cite this: J. Mater. Chem. A, 2025, 13, 11637

Efficient ethane production *via* $SnCl_4$ Lewis acid-enhanced CO_2 electroreduction in a flow cell electrolyser†

Sankeerthana Bellamkonda, *[ab] Ian Brewis, [a] Venkateswara Rao Gedela,[a] Rana Faisal Shahzad,[a] Mohamed Mamlouk [b] and Shahid Rasul *[a]

The development of efficient and selective catalysts for electrochemical CO_2 reduction (ECR) is critical for advancing sustainable energy solutions. Here, we report a unique catalyst system based on $SnCl_4$ Lewis acid-modified Cu_2O, demonstrating enhanced performance in CO_2 electroreduction to ethane. The $SnCl_4$ modification introduces chloride ions directly onto the Cu_2O surface, creating a synergistic interaction between Sn, Cl, and Cu active sites that optimizes the electronic environment for ECR. The $SnCl_4$ catalyst was deposited on Cu_2O coated gas diffusion electrode (GDE) and tested in a flow cell electrolyser, integrating a Fumasep bipolar membrane and platinum (Pt) foil anode. This system achieved a peak faradaic efficiency of 34.8% for ethane production at −1.0 V *vs.* RHE, along with 11.3% efficiency for ethylene. Electrochemical studies revealed that the $SnCl_4$-modified Cu_2O exhibits low charge transfer resistance and high stability during prolonged electrolysis, achieving a total current density of 74.8 mA cm^{-2} with a Tafel slope of 92.3 mV dec^{-1} at 0.4 V overpotential. Mechanistic investigations, supported by density functional theory, Raman, XRD, and electrochemical impedance spectroscopy analyses, highlight the critical role of chloride ions in stabilizing CO intermediates and facilitating C–C bond formation, essential for C_2 product generation. Operating in a flow cell configuration, the system demonstrated high energy efficiency and selectivity, establishing the $SnCl_4$-modified Cu_2O (CTC) as a promising catalyst for ECR. These findings offer a scalable and economically viable pathway for renewable hydrocarbon production, paving the way for practical applications in carbon-neutral energy cycles.

Received 8th January 2025
Accepted 11th March 2025

DOI: 10.1039/d5ta00176e

rsc.li/materials-a

1. Introduction

Concerns about global warming and a potential energy crisis have driven the search for innovative methods to convert CO_2, a prominent greenhouse gas emitted by fossil fuel combustion, back into fuels or other valuable molecules.[1] Reducing CO_2 emissions is critical for addressing the challenges of climate change. Carbon capture, utilization, and storage (CCUS) technologies are gaining traction to achieve net-zero emissions by converting CO_2 into useful products.[2–4] CO_2 electrolysis is particularly promising, using renewable energy to turn CO_2 into chemicals and fuels, offering a sustainable route to carbon neutrality. This approach has the potential to significantly reduce emissions and facilitate the transition to a greener future.[5] A key strategy for achieving a carbon-neutral energy cycle involves powering electrochemical CO_2 reduction (ECR) using renewable energy sources.[6] However, ECR faces significant energy barriers due to the strong chemical inertness of CO_2 molecules and the complex multi-electron transfer processes involved.[7–9] ECR can yield various C1 products, including CO and CH_4, as well as C_2 products such as ethylene (C_2H_4), ethanol (C_2H_5OH), and ethane (C_2H_6).[10,11] Ethane, in particular, stands out due to its high energy density of approximately 1.43 MJ mol^{-1}, making it a highly desirable product for energy storage and other applications.[12,13]

However, achieving high selectivity for ethane in electrochemical CO_2 reduction is challenging, primarily due to the intricate control required for C–C bond formation and subsequent hydrogenation processes. The selective production of ethane is particularly difficult because it requires not only the formation of C–C bonds but also precise control over the hydrogenation steps to avoid over-reduction to methane or under-reduction, leading to less valuable products.[14,15] Therefore, the development of high-performance electrocatalysts that can steer the reaction pathways towards ethane while minimising the production of undesired byproducts is crucial. Despite significant advancements,[16–19] directing reaction pathways toward desirable products like ethane and reducing

[a]School of Engineering and Environment, Northumbria University, Newcastle upon Tyne, UK. E-mail: sankeerthana999@gmail.com; shahid.rasul@northumbria.ac.uk; Tel: +44 7471042866; +91 9445435743

[b]School of Engineering, Newcastle University, Newcastle upon Tyne, UK

† Electronic supplementary information (ESI) available: 3D drawing of the CO_2 electrolyser, synthesis and faradaic efficiencies of Cu_3Sn and Cu_2O, XRD, XPS, Raman, and SEM analyses of Cu_2O and post-CO_2 electrolysed CTC-65, and simulated band structures. See DOI: https://doi.org/10.1039/d5ta00176e

reaction potentials remain substantial challenges, necessitating the development of advanced electrocatalysts with improved product selectivity and catalytic activity.

One established strategy for enhancing ECR performance is modifying catalyst surfaces with functional additives.[19] This can be achieved either by directly altering the electronic properties of the catalyst surface or indirectly by affecting binding strengths through adsorbate–adsorbate interactions. For example, Kim *et al.*[20] demonstrated that the CO selectivity and reduced overpotential of Ag nanoparticles on carbon substrates could be enhanced using different anchoring agents. They suggested that the improved CO selectivity was due to the localized unpaired electrons of the anchoring agent at the surface state of Ag. Additionally, Au surfaces functionalized with imidazolium ions and thiol-tethered ligands have been investigated for their ability to control the selectivity of ECR products.[21]

Anion adsorption on metal catalysts has also been shown to improve ECR performance. Numerous studies have demonstrated that the presence of chloride anions enhances CO selectivity while suppressing the hydrogen evolution reaction (HER).[21–23] Jihun Oh revealed that chloride-adsorbed Au electrodes exhibited four times the CO selectivity of bare Au at −0.39 V.[24] Their studies, both theoretical and experimental, elucidated the role of adsorbed chloride on the Au surface in influencing ECR activity and selectivity. Similarly, adsorbed chloride on Ag surfaces has been shown to boost ECR intrinsic activity and selectivity by minimising side reactions associated with the HER.[25] Zn-based catalysts[26] have also been extensively investigated in chloride anion-containing electrolytes. It has been hypothesized that the increased CO faradaic efficiency results from chloride anion adsorption on the electrode surface, which preferentially facilitates electron transfer from CO_2 to intermediates,[26] thereby enhancing CO generation selectivity. For instance, a chloride anion-linked Ag nanocoral structure exhibited 32 times greater ECR activity compared to pure Ag.[27] While halide adsorption on Cu-based catalysts has been explored, the role of chloride ions in tuning ECR pathways for selective ethane formation remains underexplored, particularly when introduced *via* direct catalyst modification rather than electrolyte-based approaches.

To address this gap, this study employs a novel surface modification strategy using $SnCl_4$ as a Lewis acid to enhance the ECR performance of Cu_2O. Unlike previous studies that introduce halide-based salts into the electrolyte to investigate halide adsorption effects,[28–31] this work directly anchors $SnCl_4$ onto the electrode surface rather than relying on dissolved Cl^- ions. This approach ensures controlled and localized chloride adsorption, avoiding fluctuations in Cl^- concentration associated with electrolyte-based methods, which can lead to uncontrolled adsorption–desorption behavior, unpredictable competitive interactions with reaction intermediates, and potential electrode degradation. By modifying Cu_2O with $SnCl_4$, chloride ions are directly bound to the catalyst surface, providing a stable and reproducible environment for systematically investigating their role in CO_2 reduction. This method allows for a more precise understanding of the impact of chloride species on catalytic performance, particularly in steering the reaction pathway toward ethane formation.

In this study, we systematically investigate the role of chloride ions on Cu–Sn electrodes (copper tin chloride, CTC) for ECR. First, we experimentally evaluate the influence of adsorbed chloride by functionalizing the Cu_2O surface *via* $SnCl_4$ deposition and analyse its effect on ECR activity and product selectivity. Special attention is given to ethane formation, examining how chloride anions influence C–C bond formation and hydrogenation pathways. We then propose an ECR mechanism highlighting the significance of chloride ions in selectively driving CO_2 reduction toward hydrocarbons, particularly enhancing ethane production. The findings from this work provide key insights into catalyst design strategies for optimizing electrochemical CO_2 reduction to C_2 hydrocarbons, offering a scalable pathway for sustainable fuel synthesis.

2. Experimental section

2.1 Materials

Cuprous oxide (Cu_2O, Merck), a carbon gas diffusion layer (Fuel Cell Systems), and tin(IV) chloride pentahydrate (Merck) were used as precursors for the Sn and Cl deposition on the Cu_2O-coated gas diffusion electrode. Potassium hydroxide (KOH, Merck) was used to prepare the electrolytes. Deionized water was used to prepare all solutions and to rinse the samples and glassware.

2.2 Electrode fabrication

2.2.1 Preparation of Cu_2O/GDL electrodes. Cu_2O–GDL was prepared by brush-coating commercial Cu_2O particles (EPRUI Nanoparticles & Microspheres Co. Ltd) onto the surface of a 1 cm × 1 cm commercial GDL (Fuel Cell Systems). Specifically, 15 mg of Cu_2O was dispersed in 200 μL of isopropanol (>99.8%, VWR Chemicals) and 66 μL of a 5 wt% Nafion suspension (Sigma-Aldrich) to create the catalyst ink. This mixture was sonicated for 20 minutes, and the ink was then coated on a 1 cm^2 GDL surface with a brush, using a layer-by-layer coating technique. After each layer, the coating was dried at 40–50 °C for 1–3 minutes. This process was repeated until the target catalyst loading of 4–5 mg cm^{-2} was achieved.

2.2.2 Preparation of Cu_2O/$SnCl_4$/GDL (CTC) electrodes. The CTC electrodes are finally prepared by loading 20–80 μL of $SnCl_4$ Lewis acid onto the Cu_2O coated GDL using a micropipette, and these CTC electrodes were dried at room temperature for one minute. These electrodes were then directly used as cathodes for CO_2 electrolysis in a flow cell electrolyser. The Cu_3Sn (Sn deposited Cu_2O) catalyst has been synthesised using an *in situ* electrochemical simultaneous deposition method, as shown in Fig. S1 in the ESI.†

2.3 Electrode characterization

Scanning electron microscopy (SEM, Hitachi S-4800) was used to examine the morphologies of the synthesized catalysts. The elemental composition and mapping of samples were analysed with energy-dispersive X-ray spectroscopy (EDS, Oxford Instruments). X-ray diffraction (XRD) characterization was performed using a Rigaku Miniflex 600 benchtop sixth-generation X-ray diffractometer. The X-ray photoelectron spectroscopy (XPS)

spectra were recorded using an ESCA+ (Omicron Nanotechnology, Oxford Instrument, Germany) equipped with a monochromatic aluminum source (Al Kα radiation $\hbar\nu = 1486.6$ eV), operated at 15 kV and 20 mA. The C 1s binding energy of 284.6 eV is taken as a reference. The Raman measurements were obtained at room temperature using a BRUKER RFS 27 with a 627 nm laser source.

2.4 Electrochemical measurements

The electrochemical measurements were performed using an Autolab potentiostat/galvanostat (Metrohm Autolab PGSTAT302N). Ag/AgCl and Pt foil were used as the reference and counter electrodes, respectively. The reference electrode was converted to RHE using the following equation:

$$E_{RHE} = E_{Ag/AgCl} + 0.1976 + 0.0591 \times pH$$

We investigated the ECR catalysts using a lab-customised 3D-printed electrolyser flow cell, as shown in Fig. S2 in the ESI.† The catalysts were deposited on a carbon paper GDL substrate, with Ag/AgCl and Pt foil serving as the reference and counter electrodes, respectively. CO_2 gas was introduced into the gas chamber *via* a gas inlet and diffused across the GDL to reach the catalyst layer. The CO_2 gas flow rate was maintained at a constant 50 mL min^{-1} using a flow meter (Cole-Parmer TMR1-010462). A Fumasep FBM bipolar membrane was used between the cathodic and anodic compartments to allow the transfer of cations. Platinum foil was used as the anode. After 30 minutes of CO_2 electrolysis, the gas products were collected from the gas outlet for GC measurements, and the catholyte was collected for liquid product analysis using ion chromatography. To investigate the ECR behaviour of CTC-65 electrodes, we conducted chronoamperometry (CA) tests for 1 hour at potentials of −0.5 V, −0.65 V, −0.75 V, −0.85 V, and −1.00 V *vs.* RHE. The faradaic efficiency (FE) of the electrochemical reaction was estimated from the CA measurements by considering the input charge, the duration of the electrochemical process, and the quantification of the gaseous/liquid products and their molar masses.

2.5 CO_2 reduction measurements and product analyses

In the CO_2 recycling tests, a lab-customized electrochemical cell with three compartments (for the working, reference, and counter electrodes) was used. Each cathodic and anodic compartment contained 6 mL of 1 M KOH electrolyte. The CO_2 reduction reaction was performed at various potentials in CO_2-saturated 1 M KOH (pH = 13.8, measured with an Accumet AB15 pH meter) for 60 minutes, with the electrolyte remaining static (no peristaltic pump was used). After electrolysis, a 1 mL gas sample was taken through a septum port using a gas-tight syringe and injected into a gas chromatograph (GC) (Shimadzu 2014) to quantify the amounts of CO, H_2, and hydrocarbons. Ion chromatography (Thermo Fisher Dionex ICS-1600) was used to analyse the liquid products.

The FE was calculated after quantifying the formate as follows:

$$FE = (2 \times F \times n)/Q$$

where F represents the Faraday constant (96 485 C mol^{-1}), n is the concentration of formate (mol), and Q is the total charge during the reaction time. The gaseous products were quantified using a gas chromatograph (Shimadzu 2014) equipped with a thermal conductivity detector (TCD) and a flame ionization detector (FID) with a methanizer. The TCD was used to detect hydrogen (H_2), while the FID was used to detect carbon monoxide (CO) and other carbon-based gaseous products. Argon gas was used as the carrier gas. Prior to the CO_2 reduction studies, the GC was calibrated with known concentrations of both CO, CH_4, C_2H_4, C_2H_6 and H_2. After quantification of the gaseous products, the faradaic efficiency was calculated using the following equation:[32]

$$FE\ (g) = (n \times x \times F \times v \times P)/(R \times T \times I)$$

where n = number of electrons required to convert 1 mol of a particular product. x = concentration of obtained gaseous products, F = Faraday constant (96 485 C mol^{-1}), $\theta_{flowrate}$ = volumetric flow rate, $P = 101\,325$ Pa, R = gas constant (8.314 J mol^{-1} K^{-1}), $T = 298$ K, and I = average current density after reaching a steady state (A).

2.6 Computational methods

First principles, plane wave self-consistent field calculations were executed using the generalized gradient approximation (GGA) method using QUANTUM ESPRESSO.[33a] The Perdew–Burke–Ernzerhof (PBE) exchange–correlation functional with projector-augmented wave type pseudopotentials was used to treat electron core interactions in all the atoms. A kinetic energy and charge density cut-off of 30 Ry and 300 Ry, respectively, were applied for better convergence. The slab models for Cu contained four atomic layers with the bottom two layers fixed, while the slab models for CTC contained 1 Sn atom and 2 Cl atoms on the surface of 5 nuclear layers of Cu with the bottom two layers fixed. In the aperiodic directions, at least 15 Å vacuum space was added to each model to avoid interactions between neighbouring images. The structural coordinates of the relaxed Cu, CTC, CTC–CO and CTC–CO–K slabs are given in the ESI. Complete structural relaxation with a $6 \times 6 \times 1$ k-mesh was performed until the total energy was converged to 10^{-5} eV and the residual forces on all unconstrained atoms were less than 0.02 eV $Å^{-1}$. The conducting nature of the system was incorporated through the tetrahedron method in calculating the electronic properties.[33b] The binding energy of CO and K was computed as the difference between the energy of the composite system and the sum of the energies of the clean surface and uncoordinated adsorbate.

3. Results and discussion

3.1 Electrochemical CO_2 reduction in an electrolyser flow cell

We analysed loading-dependent ECR performance by drop-casting various amounts (20–80 μL) of $SnCl_4 \cdot 5H_2O$ Lewis acid onto Cu_2O GD electrodes, and the electrodes are denoted as CTC-20, CTC-42, CTC-65, and CTC-80. The electrodes are

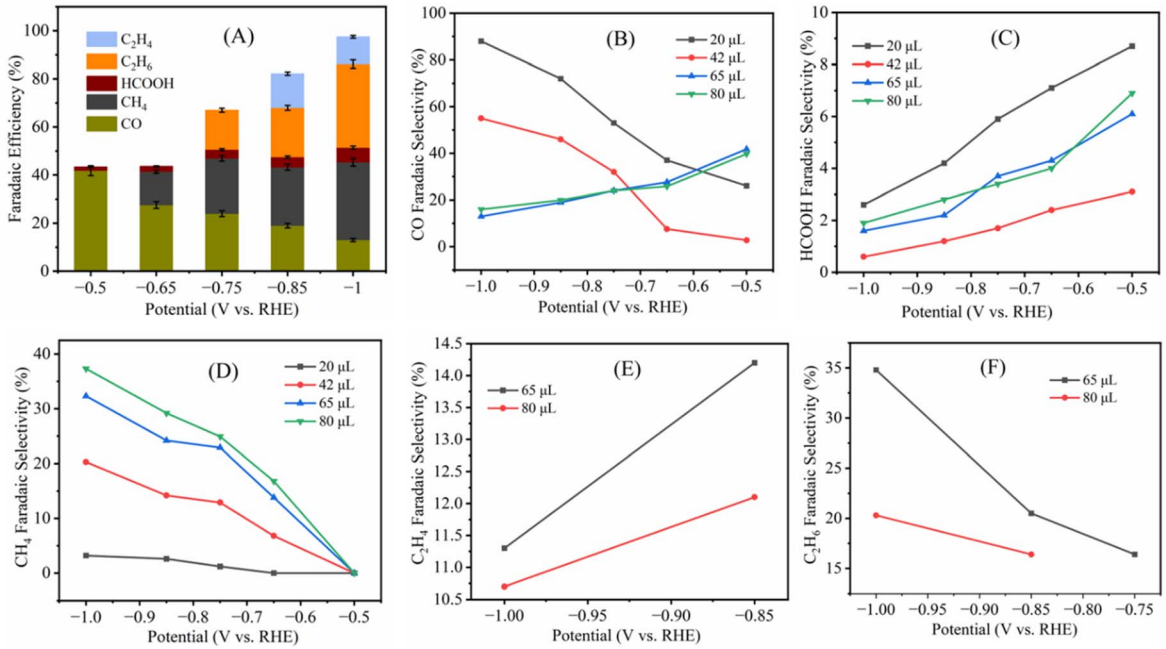

Fig. 1 Faradaic efficiency of different products (C_2H_4, C_2H_6, HCOOH, CH_4, and CO) as a function of potential for the electrode CTC-65 during electrochemical reduction using a flow cell electrolyser (A); and faradaic selectivity of CO (B); HCOOH (C); CH_4 (D); C_2H_4 (E); and C_2H_6 (F) as a function of potential for the electrodes loaded with different volumes of $SnCl_4$ Lewis acid on the Cu_2O GDE.

named based on the volume of $SnCl_4$ deposited onto Cu_2O GDEs. Briefly, the electrochemical performance of the CTC electrodes is determined by bubbling CO_2 into the cathode compartment electrolyte (catholyte) at a flow rate of 50 mL min^{-1}, and a constant potential was applied to the $SnCl_4$/Cu_2O cathodes with a potentiostat. The effluent gas stream was collected, and the reaction products were analysed every 30 min with gas and ion chromatography.

The distribution of the gaseous products obtained during the CO_2 electrochemical reduction at cathodic potentials ranging from −0.5 to −1.0 V *vs.* RHE is shown in Fig. 1. It is evident that only minor differences exist in the faradaic efficiency (FE) of the gaseous products between the electrodes deposited with different loadings of $SnCl_4$. Carbon monoxide (CO), methane (CH_4), ethylene (C_2H_4) and some ethane (C_2H_6) were gaseous products observed from CO_2 electrochemical reduction. CO desorbs from the surface and is a well-known intermediate for the formation of C_2H_6, C_2H_4 and CH_4. Ethane is the major product among the hydrocarbons for CTC-65 and CTC-80 electrodes with a small variation in the ethane/methane ratio observed. Ethane formation was detected with low FE for CTC-65 investigated at −0.75 V *vs.* RHE. Fig. 1A demonstrates that as the CTC-65 electrode potential becomes more negative, the FE for C_2H_4 and C_2H_6 increases, while the efficiencies for CH_4, formic acid (HCOOH), and CO decline or remain relatively constant. Fig. 1B and C further illustrate the decreasing selectivity for CO and HCOOH, respectively, at more negative potentials, emphasizing that lower $SnCl_4$ loading on the Cu_2O GDE led to a more pronounced decrease in selectivity. Fig. 1D shows the declining trend of CH_4 FE selectivity as the potential becomes more negative, specifically at higher loadings of $SnCl_4$ Lewis acid. In contrast, Fig. 1E demonstrates that C_2H_4 selectivity increases with more negative potentials, particularly at a $SnCl_4$ loading volume of 65 μL. Finally, Fig. 1F illustrates a decline in ethane selectivity with more negative potentials for both reagent volumes, although selectivity is higher at a lower volume (65 μL). Overall, the optimal loading of $SnCl_4$ for the electrochemical reduction of CO_2 is 65 μL, which serves as the basis for the exploration of the CTC-65 GDE. In contrast, the bare Cu_2O GDE primarily produces C1 products such as CO and CH_4, and the Cu_3Sn (Sn deposited Cu_2O) GDE shows improved selectivity for HCOOH and CO due to the presence of Sn, which favours formate formation. The FEs of bare Cu_2O and Cu_3Sn GDEs are given in Fig. S3.†

The Cu_2O/$SnCl_4$ GDEs are fabricated by drop casting 65 μL of $SnCl_4 \cdot 5H_2O$ solution on a Cu_2O GDE and named CTC-65. The photographs of the as-fabricated Cu_2O, pre-electrolysed CTC-65 and post-CO_2 electrolysed CTC-65 electrodes are shown in Fig. 2. The CTC-65 electrode becomes whitish after coating the

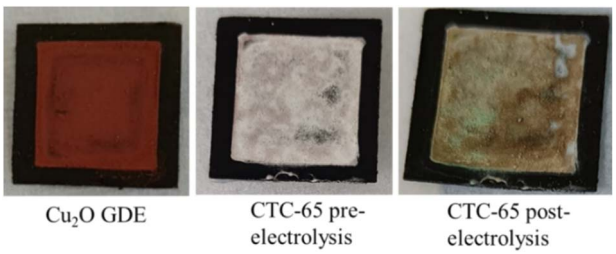

Fig. 2 Photographs of the appearance of Cu_2O and CTC-65 and post-CO_2 electrolysed CTC-65 coated on gas diffusion layer (GDL) electrodes.

brick-reddish Cu_2O, which reveals the deposition of chloride on the electrode.

3.2 Morphological, structural and electrochemical analysis

As shown in Fig. 3, the SEM images and EDS analysis provide insight into the structural and compositional characteristics of the Cu_2O and pre-electrolysed CTC catalysts. The SEM images and EDS analysis of the post-electrolysed CTC catalysts are given in Fig. S4 and S5.† The SEM image of Cu_2O reveals a relatively smooth surface morphology, which serves as the initial substrate for further modifications. In contrast, the pre-electrolysed CTC-65 exhibits a more complex, roughened surface with well-defined nanoscale structures, suggesting an increased surface area and enhanced active sites, which are beneficial for catalytic performance. The post-electrolysed CTC morphology in Fig. S4† shows the retention of these structural features, although some aggregation and possible morphology changes are visible, indicating that the catalyst has undergone structural adjustments due to electrochemical CO_2 cycling. The elemental mapping from EDS confirms the presence of Cu, Sn, and Cl as the primary components in the fresh CTC-65 catalyst, with high concentrations of Sn and Cl distributed evenly, suggesting successful incorporation of these elements into the catalyst structure. The EDS spectrum further corroborates the composition, showing peaks for Sn, Cl, Cu, and O, consistent with the intended CTC structure. Additionally, the EDS analysis of post-CO_2 electrolysed CTC-65 (Fig. S5†) confirms the retention of Sn and Cl species, suggesting the structural stability of the catalyst under electrolysis conditions, reinforcing its suitability for sustained CO_2 reduction.

In order to find the crystallization transformation of CTC-65 electrodes, we performed XRD characterization to study the electrode before electrochemical measurements. Fig. 4A shows XRD patterns of CTC-65 before the CO_2 electrolysis treatment. The XRD profiles of the bare Cu_2O GDE, GDL, and post-CO_2 electrolysed CTC-65 are given in Fig. S6.† For Cu_2O, the peaks at 29.49°, 36.48°, 42.55°, 61.42°, and 73.69° correspond to (110), (111), (200), (220), and (311) planes, respectively.[34–36] After adding $SnCl_4$ onto Cu_2O, the peaks corresponding to the (111) and (200) planes of Cu_2O diminish and shift to 35.86° and 40.16° with the disappearance of the remaining corresponding Cu_2O peaks. This demonstrates that the exposure of the Cu_2O layer is decreased due to the addition of $SnCl_4 \cdot 5H_2O$ over its surface. Furthermore, the shift in the peaks indicates that there is an interaction between Cu_2O and Cl or Sn, which is in accordance with the appearance of additional sharp peaks related to the mixed phases of $SnCl_2 \cdot 2H_2O$, Sn(OH)Cl, $Sn_2(OH)_2O$, CuCl and $Cu_2(OH)_3Cl$.[37–40]

As $SnCl_4 \cdot 5H_2O$ is highly hygroscopic, it readily absorbs atmospheric moisture, leading to spontaneous hydrolysis and

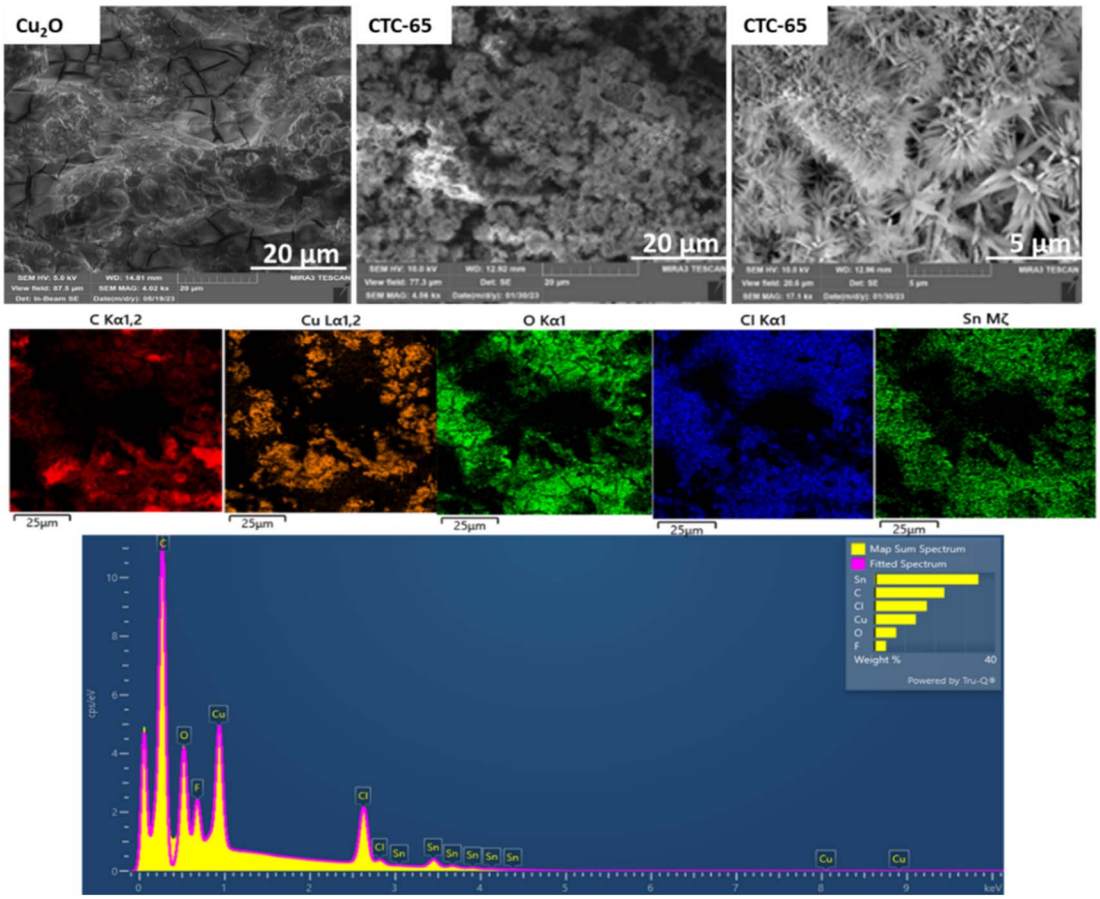

Fig. 3 Scanning electron microscopy images of Cu_2O and pre-CO_2 electrolysed CTC-65 and its elemental mapping.

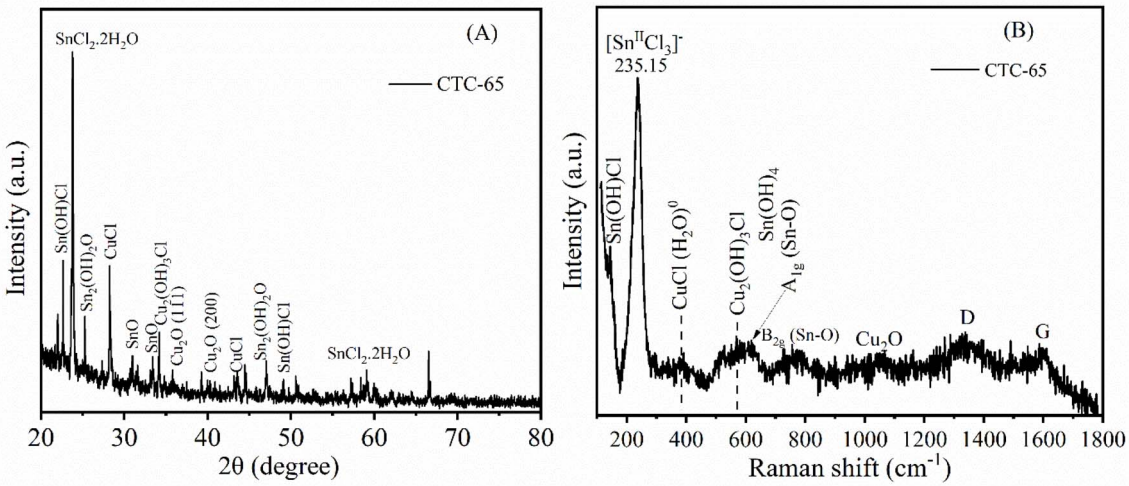

Fig. 4 (A) Powder XRD patterns and (B) Raman signals of CTC-65 electrodes recorded at room temperature.

the formation of hydrolysed tin and chloride species. Upon exposure to air, $SnCl_4$ undergoes hydrolysis, forming compounds such as $Sn(OH)Cl_3$ and $Sn(OH)_2Cl_2$. When deposited onto the Cu_2O surface, these hydrolysed species interact with Cu, resulting in the formation of Sn–O–Cu and Cu–Cl bonds, which modify the electronic environment of the electrode. This is evident in the XRD patterns, where multiple phases coexist within the same compound, indicating the structural and compositional changes induced by $SnCl_4$ modification. The possible mechanisms leading to the formation of these phases are as follows:

$$SnCl_4 + H_2O \rightarrow Sn(OH)Cl_3 + HCl$$

$$Sn(OH)Cl_3 + H_2O \rightarrow Sn(OH)_2Cl_2 + HCl$$

$$Cu_2O + 3H_2O + Cl \rightarrow Cu_2(OH)_3Cl + H^+$$

These structural transformations are further confirmed by Raman analysis, as shown in Fig. 4B, indicating the formation of Cu–Cl, Sn–OH–Cl, and Cu–OH–Cl bonds on the surface of the CTC-65 electrode. The prominent peak at 235.15 cm^{-1} in the Raman spectrum corresponds to the $Sn(II)Cl_3^-$ species, suggesting the presence of tin chloride complexes that are essential for catalytic performance.[38,41] Additional peaks around 400–600 cm^{-1} are attributed to CuCl and $Cu_2(OH)_3Cl$ phases,[42] as well as Cu_2O, indicating that copper species are present in different oxidation states and environments within the CTC-65 GDE. The observed Cu_2O signals suggest the incorporation of copper oxides, which may contribute to the stability and activity of the catalyst. The peaks around 800–1000 cm^{-1} correspond to $Sn(OH)_4$ and Sn–O vibrations,[43] demonstrating that tin is integrated in both hydroxylated and oxide forms, which may play a role in facilitating CO_2 adsorption and activation. The weak D and G bands observed at higher Raman shifts (~1300–1600 cm^{-1}) are associated with carbonaceous materials, possibly originating from the carbon GDL. This indicates the presence of multiple active species, including CuCl, Cu_2O, and $Sn(OH)_4$, which together create a mixed catalytic surface that supports the electrochemical reduction of CO_2 by providing various active sites for intermediate stabilization and electron transfer. The results from powder XRD and Raman confirm that chemical transformations occurred on the surface of the Cu_2O GDE immediately after drop casting 65 μL of $SnCl_4 \cdot 5H_2O$ Lewis acid. We speculate that due to its hygroscopic nature, $SnCl_4 \cdot 5H_2O$ rapidly reacted with nearby species upon contact, resulting in the formation of hydroxychlorides, metal chlorides, and metal hydroxides. The Raman signal at 235.15 cm^{-1} in the Raman spectrum of the post-CO_2-electrolyzed CTC-65 electrode (Fig. S7†) confirms the stability and retention of Cl and Sn on the CTC-65 surface after electrolysis.

The XPS spectra presented in Fig. 5 reveal detailed insights into the chemical state changes of Cu, Sn, Cl, and other elements on the CTC-65 catalysts before and after CO_2 electrolysis. Fig. 5A and B show the Cu 2p spectra, where the shift in lower binding energies and the reduced intensity of the satellite peaks after electrolysis indicate the reduction of Cu^{2+} to Cu^0, confirming the transformation of Cu_2O to a more metallic Cu state.[44–46] This change in the oxidation state suggests enhanced electronic conductivity and improved CO adsorption on metallic Cu sites, promoting C–C coupling. In Fig. 5C, the Sn 3d spectra show minimal shift in binding energy, indicating the stability of Sn species during CO_2 reduction.[47,48] The presence of Sn in the +4-oxidation state before and after electrolysis suggests that Sn acts as an electronic modulator, maintaining a consistent electronic environment that stabilizes CO intermediates, thereby enhancing C_2 product selectivity.[49] Fig. 5D displays the Cl 2p spectra, where the consistent binding energies before and after electrolysis confirm that chloride ions remain anchored to the catalyst surface, preventing leaching during prolonged CO_2 reduction.[34,50] This stable Cl environment is crucial for suppressing the hydrogen evolution reaction (HER) and increasing the local CO concentration, favoring C–C coupling. The C 1s spectra in Fig. 5E reveal the presence of C–C/

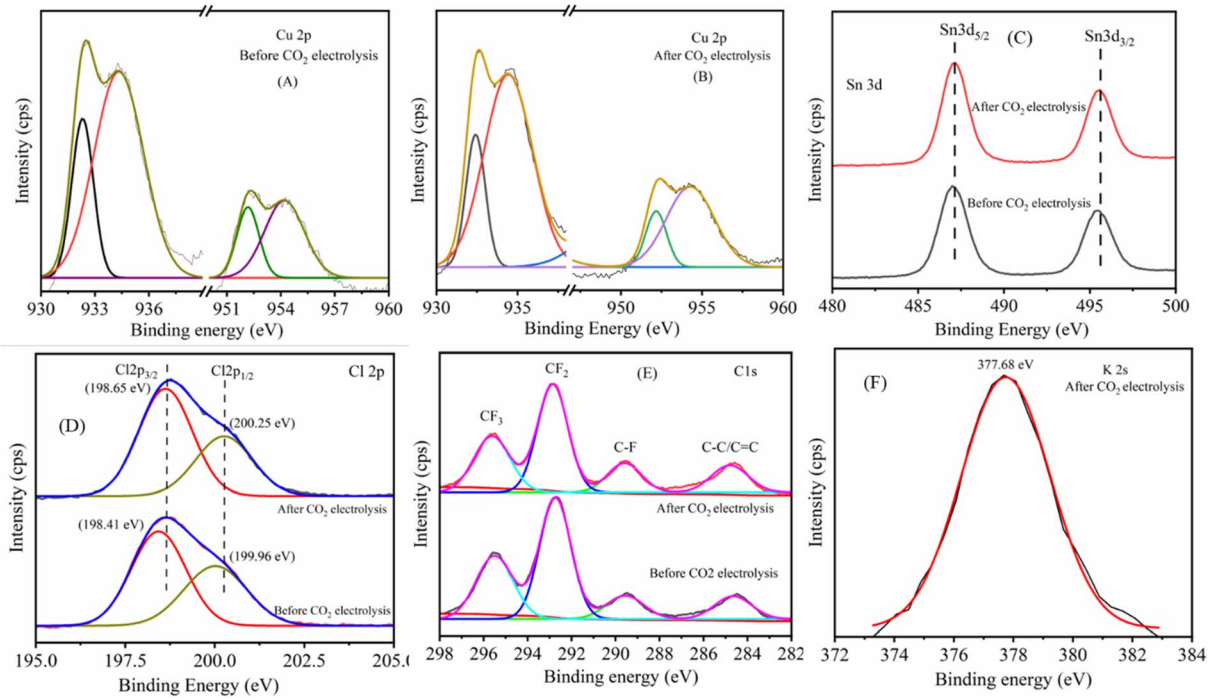

Fig. 5 XPS analysis of the CTC-65 electrode before and after CO_2 electrolysis, showing the spectra of Cu 2p (A and B), Sn 3d (C), Cl 2p (D), C 1s (E), and K 2s (F).

C=C and C–F species of the PTFE coated GDL,[51,52] and C–F species are from the PTFE coated GDL.[53,54]

Fig. 5F shows the K 2s spectra of post-CO_2 electrolysed CTC-65, confirming the adsorption of K^+ ions from the KOH electrolyte, which likely contribute to electrostatic stabilisation of CO_2 reduction intermediates.[55] The presence of K^+ ions emphasizes the significance of the KOH electrolyte in facilitating CO_2 electrolysis using CTC-type halide-based electrocatalysts. These observations collectively demonstrate the synergistic roles of Sn and Cl in stabilising key intermediates and optimising the electronic structure of the CTC catalysts, leading to enhanced selectivity and efficiency for C_2 hydrocarbon production. XPS analysis further confirms the successful incorporation of Cu, Sn, and Cl species into the $Cu_2O/SnCl_4$ GDE, which is in correspondence with the SEM elemental mapping.

3.3 Electrochemical CO_2 reduction activity

To explore the electrochemical properties of the Cu_2O and CTC-65 electrodes, cyclic voltammetry was performed in a three-electrode system (Fig. 6A and B). The cyclic voltammograms of Cu_2O and CTC-65 were recorded in 1 M KOH electrolyte in the potential range from −2.5 V to +1.0 V (*vs.* Ag/AgCl) with a scan rate of 50 mV s^{-1}. In Fig. 6B, Cu_2O shows two reduction peaks with cathodic peak potential (E_{pc}) values of −0.45 and −0.98 V *vs.* Ag/AgCl, which can be assigned to the reduction of Cu^{2+}/Cu^+ and Cu^+/Cu, respectively.[56] During the reverse scan, two oxidation peaks at −0.36 and −0.05 V *vs.* Ag/AgCl were observed. The first anodic peak (E_{pa} − 0.37 V) is associated with the oxidation peak of Cu/Cu^+, while the second peak (−0.05 V) is associated with Cu^+/Cu^{2+}. For the CTC-65 electrode, more pronounced cathodic peaks related to Cu^{2+}/Cu^+ and Cu^+/Cu and anodic peaks related to Cu/Cu^+ and Cu^+/Cu^{2+} are positively shifted with an additional peak at −0.74 V *vs.* Ag/AgCl corresponding to reduction of Sn (Sn^{2+}/Sn).[56] The positive shift in the redox peaks of Cu in CTC-65 can be ascribed to the interaction of Cl^- ions with the Cu electrode.

The electrochemical CO_2 reduction activity of CTC-65 was evaluated using CV in 1 M KOH aqueous electrolyte, providing insights into its superior catalytic performance. As shown in the CV curves collected in CO_2- and N_2-saturated electrolytes (Fig. 6A), CTC-65 exhibits significantly higher current density (232 mA cm^{-2} at −1.0 V_{RHE}) compared to the Cu_2O GDE, demonstrating its enhanced activity for ECR. In the CO_2-saturated electrolyte, a pronounced increase in current density is observed for CTC-65, highlighting its efficient catalytic activity toward ECR. The reduction activity was further evaluated as the potential was scanned toward negative values. A reduced current density was initially observed, attributed to the competition between the HER and ECR. However, a sharp increase in current density was recorded at potentials more negative than −0.45 V (*vs.* RHE), confirming the activation of ECR on the CTC-65 electrode. Notably, the current density significantly increased at potentials beyond −0.75 V (*vs.* RHE), where electrochemical CO_2 reduction becomes dominant, as Cl^- ions play a dual role. At lower overpotentials, Cl^- suppresses competing reactions such as the HER, delaying the onset of reduction activity, but at higher overpotentials, it enhances the reduction of CO_2, enabling the formation of hydrocarbons.

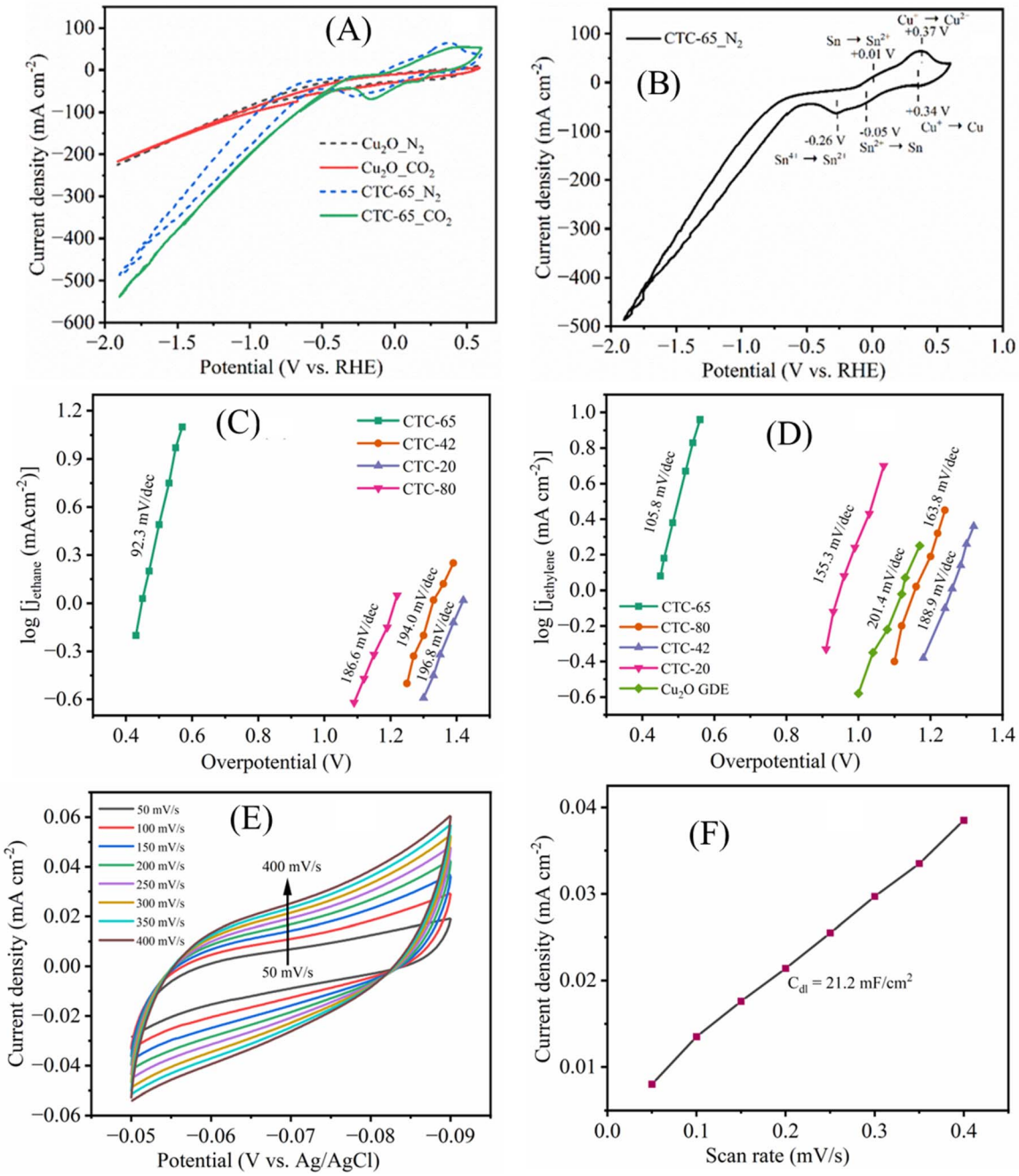

Fig. 6 (A) CV polarization curves of Cu_2O and CTC-65 electrodes scanned in the potential range of −2.0 to +0.5 V_{RHE} with a 50 mV s^{-1} scan rate under N_2 and CO_2 flows in 1 M KOH electrolyte; and (B) cyclic voltammogram of CTC-65 under a N_2 flow; (C) and (D) dependence of partial current density of ethane and ethylene on overpotential; (E) electrochemical active surface area of CTC-65; and (F) electrochemical double layer capacity of the CTC-65 GDE.

This is corroborated by the low Tafel slopes for ethane and ethylene production (Fig. 6C and D), which indicate efficient charge transfer kinetics and high catalytic activity, aligning well with the faradaic efficiency (FE) results from Fig. 1. The addition of $SnCl_4$ to Cu_2O significantly boosts CO_2 reduction activity by improving the electronic environment of the catalyst and creating active sites conducive to C–C bond formation. Furthermore, the higher electrochemical double-layer capacitance (C_{dl}) of 21.2 mF cm^{-2} (Fig. 6E and F) reflects a larger electrochemical surface area, which facilitates enhanced adsorption and activation of CO_2 intermediates. These properties drive the selective production of valuable C_2 hydrocarbons, such as ethane and ethylene, confirming the superior performance of CTC-65 as a catalyst for ECR. This systematic progression of activity, selectivity, and surface area contributions provides a cohesive understanding of the role of $SnCl_4$ in transforming Cu_2O into an efficient and selective catalyst for CO_2 reduction.

Constant potential electrolysis was performed on Cu_2O and all CTC electrodes at potentials of −0.5 V, −0.65 V, −0.75 V, −0.85 V and −1.0 V (*vs.* RHE) in a gastight three-electrode CO_2 electrolyser flow cell, with their total current densities (J_{tot}) presented in Fig. 7A. The electrocatalytic CO_2 reduction results for the CTC-65 electrodes at various potentials are shown in Fig. 7B. Initially, the CTC-65 electrodes exhibited a high geometric current density, with a recorded total current density (J_{tot}) of 74.8 mA cm^{-2} for 3600 seconds at −1 V *vs.* RHE, corresponding to the reduction of $Cu_2O/SnCl_4$ to CuSn structures. Following this transformation, the electrode achieved a stable current density during electrolysis. At a potential of −0.5 V *vs.* RHE, the CTC-65 electrode demonstrated a stable J_{tot} with a FE of 41.8% for CO and 1.6% for HCOOH production. At a more negative potential of −0.65 V *vs.* RHE, J_{tot} increased, with the corresponding FEs of 27.6% for CO, 2.2% for HCOOH, and 13.7% for CH_4 production. At −0.75 V *vs.* RHE, ethane production became significant, with an FE of 16.4%, along with FEs of 24%, 22.9%, and 3.7% for CO, CH_4, and HCOOH, respectively, at an increased current density. Notably, a peak FE of 34.8% for C_2H_6 production was observed at −1 V *vs.* RHE, accompanied by an FE of 11.3% for C_2H_4 production (Fig. 1A). This corresponds to an overpotential of only 40 mV relative to the equilibrium potential for the CO_2/C_2H_6 reaction (0.554 V *vs.* RHE). Additionally, the FE for C_2H_6 production on the CTC-65 electrode remained relatively stable over time, indicating consistent catalytic activity for CO_2 reduction. These results highlight the efficiency and stability of the CTC-65 electrode in selectively converting CO_2 into C_2 hydrocarbons during electrocatalysis.

Fig. 7C illustrates the FEs of C_2 products, including both C_2H_6 and C_2H_4, generated during CO_2 electrolysis at negative potentials of 0.75 V, 0.85 V, and 1.00 V *vs.* RHE, along with their corresponding partial current densities. At −1.00 V *vs.* RHE, the partial current density for C_2 products reaches 34.48 mA cm^{-2}, indicating that C_2H_6 and C_2H_4 production accounts for nearly half of the total current density (74.8 mA cm^{-2}). This demonstrates that higher negative potentials significantly enhance the formation of C_2 products during CO_2 reduction on CTC electrodes. These results emphasize the favorable role of more negative potentials in facilitating C–C bond formation, which is crucial for achieving selective and efficient conversion of CO_2 into valuable C_2 hydrocarbons.

The EIS in Fig. 7D provides insights into the charge transfer resistance (R_{ct}) and interfacial properties of CTC-65 during CO_2 electroreduction at various cathodic potentials. The Nyquist plots exhibit a clear trend of decreasing R_{ct} as the applied potential becomes more negative, indicating enhanced charge transfer kinetics facilitated by the presence of surface-bound chloride species. At lower potentials (−0.55 V to −0.65 V), higher R_{ct} values suggest initial limitations in electron transfer, likely due to the adsorbed chloride layer restructuring the

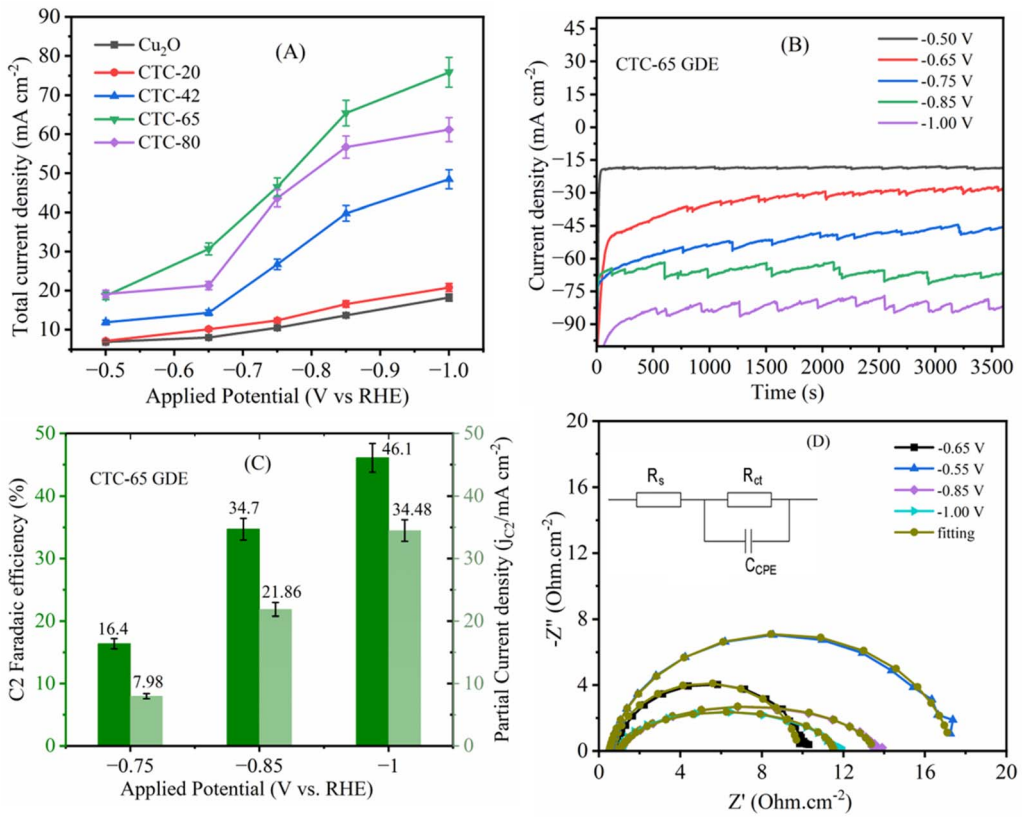

Fig. 7 (A) Total current density profiles for Cu_2O, CTC-20, CTC-42, CTC-65, and CTC-80 electrodes at various potentials; (B) constant potential electrolysis of CTC-65 at various potentials over 3600 seconds; (C) faradaic efficiencies of C2 products at various potentials with their corresponding partial current densities; and (D) electrochemical impedance spectra of the CTC-65 GDE at various potentials after CO_2 electrolysis.

electrode interface. As the potential shifts more negative (−0.85 V to −1.00 V), R_{ct} significantly decreases, corresponding to an improved catalytic process where chloride ions stabilize CO_2 reduction intermediates, particularly CO, and promote C–C coupling reactions essential for C_2 hydrocarbon formation. The equivalent circuit model (inset) includes a constant phase element (C_{CPE}), which accounts for surface heterogeneity introduced by Sn and Cl modifications. The excellent fit between experimental data and the modeled impedance response further confirms that the preloaded chloride layer modulates the electrode–electrolyte interface, reduces hydrogen evolution side reactions, and enhances CO_2 electroreduction selectivity toward ethane and ethylene. These findings corroborate faradaic efficiency trends and structural characterization (XRD, XPS, and Raman), reinforcing the role of $SnCl_4$-derived chloride in stabilizing active sites and improving long-term catalytic performance.

3.4 Mechanism involved in CO_2 reducing to hydrocarbons

From XRD, Raman, SEM, XPS and EIS analyses, it is confirmed that the CTC electrodes contain Sn and Cl species in the form of metal oxychlorides and metal hydroxychlorides. These chloride ions are physically adsorbed on the surface of CTC-65 electrodes, significantly influencing CO_2 electroreduction in an alkaline environment, as shown in Fig. 8. These adsorbed Cl^- ions create a more negative electrode environment, facilitating electron transfer to the CO_2 molecule and stabilizing the CO_2 radical. Additionally, the large ionic radius of Cl^- (0.181 nm) effectively inhibits proton adsorption, minimizing hydrogen evolution side reactions.[22,57] This aligns with the established role of M–X bonds (X = halogen and M = metal) in enhancing electron transport to CO_2 while limiting proton adsorption. This mechanism is further supported by EIS measurements, showing increased charge transfer at varying potentials. In CO_2-saturated 1 M KOH electrolyte, Cl^- ions promote a nucleophilic reaction with CO_2, enhancing local electron density and enabling CO_2 activation. According to the double-layer model, Cl^- resides on the inner Helmholtz plane, while solvated K^+ ions from the KOH electrolyte (Fig. 5F) occupy the outer Helmholtz plane, facilitating unidirectional electron flow from Cl^- to CO_2 and then to K^+. This unique double-layer configuration enhances CO_2 activation and reduction, facilitating efficient C–C coupling for hydrocarbon formation. The nucleophilic attack by Cl^- weakens the C–O bond, chemically activating CO_2 and influencing subsequent electrochemical reduction steps. This strategic modulation of the electronic environment explains the enhanced selectivity towards C_2 hydrocarbons such as ethane and ethylene, demonstrating the pivotal role of adsorbed Cl^- ions in driving CO_2 electroreduction on CTC-based electrodes.

The C_2 hydrocarbon formation pathway on the CTC catalysts is primarily governed by the CO intermediate, as supported by the faradaic efficiency trends and Tafel slope analysis. The FE results in Fig. 1 reveal that at lower potentials, CO is the dominant product, but its concentration decreases at more negative potentials, coinciding with a rise in C_2 hydrocarbon formation, including ethane and ethylene. This trend suggests that CO is consumed as an intermediate in C_2 product formation. The simultaneous decrease in CO and increase in C_2 hydrocarbons indicates a CO dimerization mechanism, where CO molecules couple to form C_2 intermediates that subsequently undergo hydrogenation to produce ethane and ethylene. The constant concentration of HCOOH across all potentials confirms that the HCOOH pathway is independent and does not contribute to C_2 hydrocarbon formation, further validating the CO dimerization pathway as the primary route for C_2 product formation.

Tafel slope analysis (Fig. 7D) provides additional mechanistic insights by revealing distinct rate-determining steps (RDSs) for ethane and ethylene. Specifically, the Tafel slopes for ethane (92.3 mV dec^{-1}) and ethylene (108.8 mV dec^{-1}) on the CTC-65 catalyst indicate efficient charge transfer kinetics but distinct RDSs for each C_2 product. The lower Tafel slope for ethane suggests that the RDS is the protonation of CO dimers, which aligns with a hydrogenation pathway. This is facilitated by Cl ions that stabilise CO intermediates, enhancing the local CO concentration and promoting hydrogenation to ethane.[58] Conversely, the higher Tafel slope for ethylene suggests that C–C coupling is the RDS, involving CO dimerization followed by dehydrogenation. This aligns with the role of Sn species, which enhance CO binding strength and promote C–C coupling through electronic modifications of the Cu surface.[59,60]

These observations indicate a CO dimerization mechanism facilitated by Cl ions, which stabilise CO intermediates and enhance local CO concentration, promoting C–C coupling. The presence of Sn species modifies the electronic structure of Cu, influencing CO binding strength and promoting hydrogenation to ethane. The distinct Tafel slopes for ethane and ethylene emphasize different rate-determining steps, confirming that ethane formation is governed by the protonation of CO dimers, while ethylene formation involves C–C coupling followed by

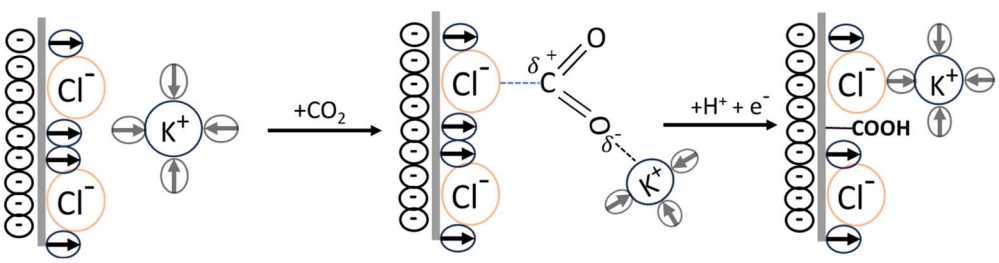

Fig. 8 Schematic representation of CO activation on CTC catalysts in KOH electrolyte.

dehydrogenation. The synergistic effects of Cu, Sn, and Cl enable efficient CO stabilisation, C–C coupling, and selective hydrogenation, leading to enhanced selectivity and efficiency for C_2 hydrocarbon formation on the CTC-65 catalyst. This coherent mechanistic pathway not only elucidates the role of CO dimerization in driving C_2 hydrocarbon formation but also underlines the strategic interplay between adsorbed Cl^- ions and Sn species in modulating the electronic and catalytic properties of the CuSnCl-based system.

Fig. 9 compares the Projected Density of States (PDOS) of the CTC electrode under three conditions: without CO, with adsorbed CO, and with CO and additional potassium (K) from the KOH electrolyte, revealing key electronic structure modifications relevant to CO_2 reduction. In the absence of CO, the PDOS is dominated by the d-orbitals of Cu and the p-orbitals of Sn and Cl near the Fermi level, indicating good electron transfer capabilities but lacking sharp features indicative of strong adsorbate interactions (Fig. 9A). Upon CO adsorption, from Fig. 9B, significant shifts occur in the density of states, with new peaks emerging from the p-orbitals of CO, interacting with the d- and p- orbitals of Cu and Cl, respectively, signifying strong binding and electronic restructuring. The addition of K further modifies the PDOS, introducing new states near the Fermi level and enhancing CO stabilization, which is crucial for promoting hydrocarbon formation (Fig. 9C). This electronic modulation facilitates selective C–C coupling and hydrogenation, optimizing the catalytic efficiency of the CuSnCl electrode for CO_2 electroreduction toward ethylene and ethane.

The charge densities for CuSnCl without adsorbates, with adsorbed CO, and with both CO and K from the KOH electrolyte reveal a progression in electron density localization, indicating the role of each adsorbate in enhancing the catalytic activity of CuSnCl for CO_2 reduction. In the bare CuSnCl profile (Fig. 9D), the electron density is uniformly distributed across the surface, indicating no specific regions of high charge concentration, which suggests limited interaction sites for catalytic intermediates. With the addition of CO (Fig. 9E), a pronounced increase in charge density is observed around the adsorbed CO molecule, indicating strong charge transfer between CO and the CuSnCl (CTC) surface. This localized electron density around CO stabilizes it as an intermediate, essential for further reduction steps. However, in Fig. 9F, where both CO and K are adsorbed on the CTC surface, an even greater concentration of electron density appears around the CO molecule and the K–CO interaction region. The presence of K enhances the stabilization of CO by further increasing electron density at the active site, which favors subsequent hydrogenation and C–C coupling steps. This sequential increase in charge density from CTC alone to CTC with CO and then to CTC with CO and K demonstrates how CO and K together create an optimized electronic environment, crucial for effective CO_2 reduction to hydrocarbons on the catalyst surface.

From Fig. 10, the stability test for the CTC-65 electrode demonstrates remarkable durability and consistent catalytic performance for CO_2 electroreduction to ethane over a 24 hour period. As shown in Fig. 10, J_{total} remains stable at approximately -75 mA cm^{-2} without significant fluctuations, indicating sustained catalytic activity under continuous electrolysis conditions. Simultaneously, the FE for ethane remains consistently above 30%, fluctuating slightly between 31% and 35% throughout the 24 hour duration. This steady FE suggests that the active sites on the CTC-65 electrode are stable and resist deactivation, thereby maintaining high selectivity toward ethane formation.

Collectively, the presence of Cu_2O, SnO_2, $SnCl_2 \cdot 2H_2O$, CuCl, and Sn(OH)Cl from XRD indicates that the electrode consists of multiple phases, each contributing uniquely to the catalytic process.

The XPS data complement these findings by confirming the presence of both Sn^{2+} and Sn^{4+} oxidation states and

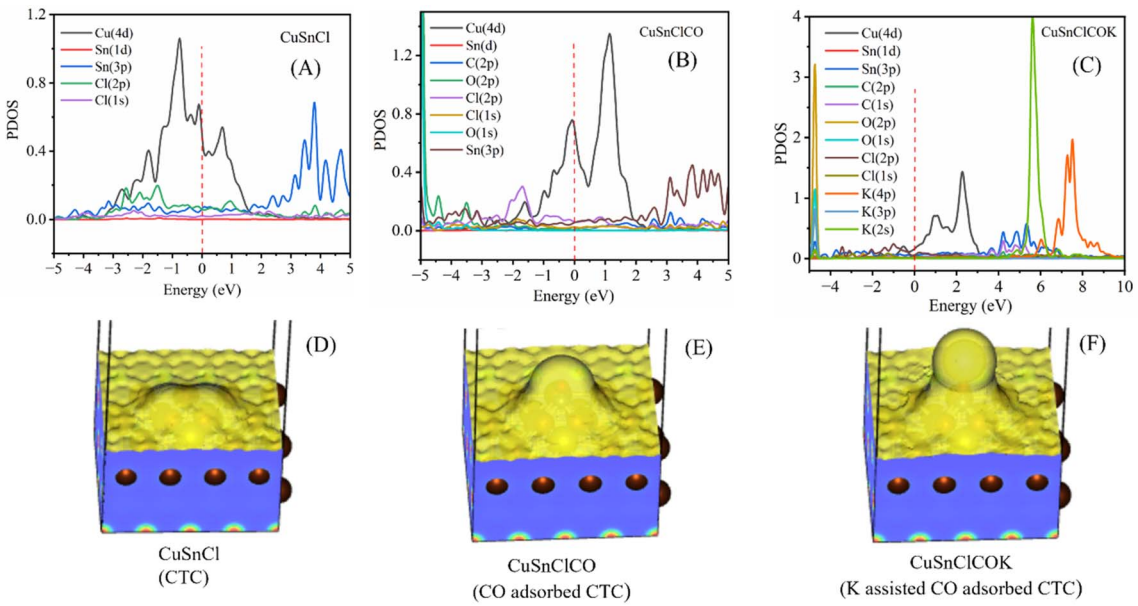

Fig. 9 PDOS spectra of CTC (A), CTC-CO (B), and CTC–CO–K (C); and charge density profiles of CTC (D), CTC-CO (E), and CTC–CO–K (F).

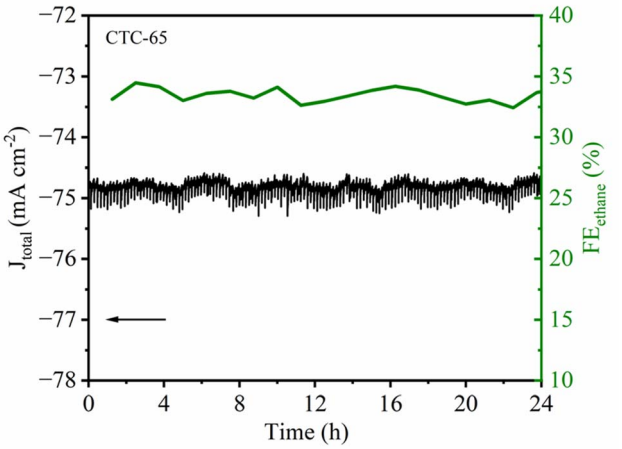

Fig. 10 24 hour stability and ethane faradaic efficiency of CTC-65 GDE at −1 V *vs.* RHE.

a predominance of Cu^+ in Cu_2O. The electronic structure likely reflects these oxidation states, showing how they contribute to the overall catalytic mechanism. Tin's dual oxidation states might explain the initial preference for single-carbon products like CO and formate (HCOOH) at less negative potentials, as these states can stabilize different reaction intermediates through electronic interactions with Cu and Cl. As the potential becomes more negative, the electronic states shift, favoring the formation of C–C bonds, leading to increased hydrocarbon production, as observed in the faradaic efficiency data.

4. Conclusion

In conclusion, this work demonstrates the significant potential of $SnCl_4$ Lewis acid-modified Cu_2O as a highly efficient and selective catalyst for electrochemical CO_2 reduction in a flow cell electrolyser configuration. By introducing chloride ions directly onto the Cu_2O surface, the synergistic interactions between Sn, Cl, and Cu active sites were optimized, facilitating the stabilization of CO intermediates and promoting C–C bond formation for the selective production of C_2 hydrocarbons. The system achieved a peak faradaic efficiency of 34.8% for ethane and 11.3% for ethylene at −1.0 V *vs.* RHE, with a stable total current density of 74.8 mA cm^{-2}. Supported by detailed mechanistic insights from PDOS, Raman, XPS, and EIS analyses, the study highlights the critical role of chloride ions in enhancing the catalytic performance. Using a Fumasep bipolar membrane and a Pt foil anode in the flow cell electrolyser, this scalable and economically viable catalyst design paves the way for sustainable CO_2 utilization and renewable hydrocarbon production, offering a promising pathway for carbon-neutral energy systems.

Data availability

All data generated during this study are included in the ESI.†

Conflicts of interest

The authors declare no competing financial interest.

Acknowledgements

This project has received funding from the Engineering & Physical Sciences Research Council – EP/X527257/1, Royce at Manchester Reference: MCAP072.

References

1 P. De Luna, *et al.*, *Science*, 2019, **364**, 350.
2 *AR6 Synthesis Report: Climate Change 2023*, 2023.
3 S. J. Davis, N. S. Lewis, M. Shaner, S. Aggarwal, D. Arent, I. L. Azevedo, S. M. Benson, T. Bradley, J. Brouwer, Y. M. Chiang, C. T. M. Clack, A. Cohen, S. Doig, J. Edmonds, P. Fennell, C. B. Field, B. Hannegan, B. M. Hodge, M. I. Hoffert, E. Ingersoll, P. Jaramillo, K. S. Lackner, K. J. Mach, M. Mastrandrea, J. Ogden, P. F. Peterson, D. L. Sanchez, D. Sperling, J. Stagner, J. E. Trancik, C. J. Yang, K. Caldeira, *et al.*, *Science*, 2018, **360**(6396), eaas9793.
4 Climate.gov, *Climate Change: Atmospheric Carbon Dioxide*, 2024.
5 European Environment Agency, *Climate Change Mitigation: Reducing Emissions*, 2024.
6 D. L. McCollum, W. Zhou, C. Bertram, H.-S. de Boer, V. Bosetti, S. Busch, J. Després, L. Drouet, J. Emmerling, M. Fay, O. Fricko, S. Fujimori, M. Gidden, M. Harmsen, D. Huppmann, G. Iyer, V. Krey, E. Kriegler, C. Nicolas, S. Pachauri, S. Parkinson, M. Poblete-Cazenave, P. Rafaj, N. Rao, J. Rozenberg, A. Schmitz, W. Schoepp, D. van Vuuren and K. Riahi, *Nat. Energy*, 2018, **3**, 589–599.
7 O. S. Bushuyev, P. De Luna, C. T. Dinh, L. Tao, G. Saur, J. van de Lagemaat, S. O. Kelley and E. H. Sargent, *Joule*, 2018, **2**, 825–832.
8 A. S. Agarwal, Y. Zhai, D. Hill and N. Sridhar, *ChemSusChem*, 2011, **4**, 1301–1310.
9 D. Higgins, C. Hahn, C. Xiang, T. F. Jaramillo and A. Z. Weber, *ACS Energy Lett.*, 2019, **4**, 317–324.
10 M. Zhong, K. Tran, Y. Min, C. Wang, Z. Wang, C. T. Dinh, P. D. Luna, Z. Yu, A. S. Rasouli, P. Brodersen, S. Sun, O. Voznyy, C. S. Tan, M. Askerka, F. Che, M. Liu, A. Seifitokaldani, Y. Pang, S. C. Lo, A. Ip, Z. Ulissi and H. S. Edward, *Nature*, 2020, **581**, 178–183.
11 S. Man, W. Jiang, X. Guo, O. Ruzimuradov, S. Mamatkulov and S. Mamatkulov, *Chem. Mater.*, 2024, **36**, 1793–1809.
12 D. W. Green and R. H. Perry, *Perry's Chemical Engineer's Handbook*, McGraw-Hill Education, 8th edn, 2007.
13 A. D. Handoko, K. W. Chan and B. S. Yeo, *ACS Energy Lett.*, 2017, **2**, 2103–2109.
14 M. Ma, K. Djanashvili and W. A. Smith, *Angew. Chem., Int. Ed.*, 2016, **55**, 6680–6684.
15 A. Dutta, M. Rahaman, N. C. Luedi and P. Broekman, *ACS Catal.*, 2016, **6**, 3804–3814.
16 K. D. Yang, W. R. Ko, J. H. Lee, S. J. Kim, H. Lee, M. H. Lee and K. T. Nam, *Angew. Chem., Int. Ed.*, 2017, **56**, 796–800.
17 J. Hussain, H. Jonsson and E. Skulason, *ACS Catal.*, 2018, **8**, 5240–5249.

18 A. Vasileff, Y. Zhu, X. Zhi, Y. Zhao, L. Ge, H. M. Chen, Y. Zheng and S. Qiao, *Angew. Chem., Int. Ed.*, 2020, **59**, 19649–19653.
19 P. Chen, P. Zhang, X. Kang, L. Zheng, G. Mo, R. Wu, J. Tai and B. Han, *J. Am. Chem. Soc.*, 2022, **144**, 14769–14777.
20 C. Kim, T. Eom, M. S. Jee, H. Jung, H. Kim, B. K. Min and Y. J. Hwang, *ACS Catal.*, 2017, **7**, 779–785.
21 T. Chen, J. Hu, K. Wang, K. Wang, G. Gan and J. Shi, *Energy Fuels*, 2021, **35**, 17784–17790.
22 M. Zhao, H. Tang, Q. Yang, Y. Gu, H. Zhu, S. Yan and Z. Zou, *ACS Appl. Mater. Interfaces*, 2020, **12**, 4565–4571.
23 J. J. Masana, B. Peng, Z. Shuai, M. Qiu and Y. Yu, *J. Mater. Chem. A*, 2022, **10**, 1086–1104.
24 M. Cho, J. T. Song, S. Back, Y. Jung and J. Oh, *ACS Catal.*, 2018, **8**, 1178–1185.
25 S. Li, X. Dong, Y. Zhao, J. Mao, W. Chen, A. Chen, Y. Song, G. Li, Z. Jiang, W. Wei and Y. Sun, *Angew. Chem.*, 2022, **134**, e202210432.
26 M. Zhao, H. Tang, Q. Yang, Y. Gu, H. Zhu, S. Yan and Z. Zou, *ACS Appl. Mater. Interfaces*, 2020, **12**, 4565–4571.
27 Y. C. Hsieh, S. D. Senanayake, Y. Zhang, W. Xu and D. E. Polyansky, *ACS Catal.*, 2015, **5**, 5349–5356.
28 A. S. Varela, W. Ju, T. Reier and P. Strasser, *ACS Catal.*, 2016, **6**, 2136–2144.
29 S. Nitopi, E. Bertheussen, S. B. Scott, X. Liu, A. K. Engstfeld, S. Horch, B. Seger, I. E. L. Stephens, K. Chan, C. Hahn, J. K. Nørskov, T. F. Jaramillo and I. Chorkendorff, *Chem. Rev.*, 2019, **119**, 7610–7672.
30 D. Gao, F. Scholten and B. R. Cuenya, *ACS Catal.*, 2017, **7**, 5112–5120.
31 T. Yuan, T. Wang, G. Zhang, W. Deng, D. Cheng, H. Gao, J. Zhao, J. Yu, P. Zhang and J. Gong, *Chem. Sci.*, 2022, **13**, 8117–8123.
32 T. Burdyny and W. A. Smith, *Energy Environ. Sci.*, 2019, **12**, 1442–1453.
33 (*a*) P. Giannozzi, S. Baroni, N. Bonini, M. Calandra, R. Car, C. Cavazzoni, D. Ceresoli, G. L. Chiarotti, M. Cococcioni, I. Dabo, A. Dal Corso, S. Fabris, G. Fratesi, S. De Gironcoli, R. Gebauer, U. Gerstmann, C. Gougoussis, A. Kokalj, M. Lazzeri, L. Martin-Samos, N. Marzari, F. Mauri, R. Mazzarello, S. Paolini, A. Pasquarello, L. Paulatto, C. Sbraccia, S. Scandolo, G. Sclauzero, A. P. Seitsonen, A. Smogunov, P. Umari and R. M. Wentzcovitch, *J. Phys.: Condens. Matter*, 2009, **21**, 395502; (*b*) F. Molani, S. Jalili and J. Schofield, *J. Mol. Model.*, 2015, **21**, 4.
34 T. Zou, F. L. P. Veenstra, E. I. Alé, R. G. Muelas, G. Zichittella, A. J. Martín, N. López and J. P. Ramírez, *Cell Rep. Phys. Sci.*, 2023, **4**, 101294.
35 Q. Zhang, L. Huang, S. Kang, C. Yin, Z. Ma, L. Cui and Y. Wang, *RSC Adv.*, 2017, **7**, 43642.
36 H. Xiang, S. Rasul, B. Hu, J. Portoles, P. Cumson and E. H. Yu, *ACS Appl. Mater. Interfaces*, 2020, **12**, 601–608.
37 C. Akyil, G. Akdas, P. Afsin and M. Urgen, *Mater. Chem. Phys.*, 2019, **221**, 263–271.
38 T. Wang, J. Chen, X. Ren, J. Zhang, J. Ding, Y. Liu, K. H. Lim, J. Wang, X. Li, H. Yang, Y. Huang, S. Kawi and B. Liu, *Angew. Chem., Int. Ed.*, 2023, **62**, e202211174.
39 J. Wang, S. Liu, X. Cao, Z. Wang, Y. Guo, X. Li, C. Liu, W. Jiang, H. Wang, N. Wang, S. Wu, H. Tao and W. Ding, *Appl. Phys. A*, 2020, **126**(44), 1–7.
40 M. Chmielová, J. Seidlerová and Z. Weiss, *Corros. Sci.*, 2003, **45**, 883–889.
41 A. F. Shihada, A. S. Abushamlesh and F. Weller, *Z. Anorg. Allg. Chem.*, 2004, **630**, 841–847.
42 X. D. Liu, X. G. Zheng, D. D. Meng, X. L. Xu and Q. X. Guo, *J. Phys.: Condens. Matter*, 2013, **25**, 256003.
43 I. M. Chou, R. Wang and J. Fang, *Geochem. Perspect. Lett.*, 2021, **20**, 1–5.
44 C. S. Gopinath, *J. Chem. Soc., Faraday Trans.*, 1996, **92**, 3605–3610.
45 Y. A. Teterin, M. I. Sosulnikov, V. I. Ozhogin, T. M. Senchenkova, N. S. Tolmacheva and L. D. Shustov, *Phys. C*, 1991, **185–189**, 837–838.
46 D. Ferrah, A. R. Haines, R. P. Galhenage, J. P. Bruce, A. D. Babore, A. Hunt, I. Waluyo and J. C. Hemminger, *ACS Catal.*, 2019, **9**, 6783–6802.
47 M. Li, X. Tian, S. Garg, T. E. Rufford, P. Zhao, Y. Wu, A. J. Yago, L. Ge, V. Rudolph and G. Wang, *ACS Appl. Mater. Interfaces*, 2020, **12**, 22760–22770.
48 E. Castillo, A. F. Pasha, Z. I. Larson and N. Dimitrov, *Mater. Adv.*, 2024, **5**, 2285–2295.
49 S. Go, W. Kwon, D. Hong, T. Lee, S. H. Oh, D. Bae, J. H. Kim, S. Lim, Y. C. Joo and D. H. Nam, *Nanoscale Horiz.*, 2024, **9**, 2295–2305.
50 L. Yu, X. Ba, M. Qiu, Y. Li, L. Shuai, W. Zhang, Z. Ren and Y. Yu, *Nano Energy*, 2019, **60**, 576–582.
51 B. Sankeerthana, R. Shanmugam and G. R. Rao, *J. Mater. Chem. A*, 2019, **7**, 3757–3771.
52 G. Cunge, B. Pelissier, O. Joubert, R. Ramos and C. Maurice, *Plasma Sources Sci. Technol.*, 2005, **14**, 599–609.
53 G. H. Yang, Y. Zhang, E. T. Kang and K. G. Neoh, *J. Phys. Chem. B*, 2003, **107**, 2780–2787.
54 K. Yang, R. Kas, W. A. Smith and T. Burdyny, *ACS Energy Lett.*, 2021, **6**, 33–40.
55 A. Pramanik, A. G. Manche, R. Clulow, P. Lightfoot and A. R. Armstrong, *Dalton Trans.*, 2022, **51**, 12467–12475.
56 A. L. S. Eh, J. Chen, S. H. Yu, G. Thangavel, X. Zhou, G. Cai, S. Li, D. H. C. Chua and P. S. Lee, *Adv. Sci.*, 2020, **7**, 1903198.
57 J. O'M. Bockris, B. E. Conway and E. Yeager, *Comprehensive Treatise of Electrochemistry*, Plenum Press, New York, 1980.
58 O. van der Heijden, S. Park, R. E. Vos, J. J. J. Eggebeen and M. T. M. Koper, *ACS Energy Lett.*, 2024, **9**, 1871–1879.
59 N. B. Watkins, Z. J. Schiffer, Y. Lai, C. B. Musgrave III, H. A. Atwater, W. A. Goddard III, T. Agapie, J. C. Peters and J. M. Gregoire, *ACS Energy Lett.*, 2023, **8**, 2185–2192.
60 M. K. Birhanu, B. Ü. Abdioglu and A. Uçar, *Catal. Sci. Technol.*, 2025, **15**, 262–317.